Spectroscopic study of Ce- and Cr-doped $LiSrAlF_6$ crystals

A. G. Kontos,[a] G. Tsaknakis, Y. S. Raptis, and A. Papayannis
Department of Physics, National Technical University of Athens, Faculty of Applied Sciences, Heroon Polytechniou 9, 15780 Zografou, Greece

E. Landulfo, S. L. Baldochi, E. Barbosa, and N. D. Vieira, Junior
Instituto de Pesquisas Energéticas e Nucleares, Centro de Lasers e Aplicações Avenida Lineu Prestes 2242, Cidade Universitária, CEP 05508-900, São Paulo, SP, Brazil

(Received 6 September 2002; accepted 9 December 2002)

Undoped, as well as Ce^{3+} and Cr^{3+} doped $LiSrAlF_6$ (LiSAF) crystals have been examined by Raman spectroscopy in order to identify the system's molecular vibrations and the role of doping. Furthermore the electron spin resonance (ESR) spectroscopic technique has been used to study the distortions of the local crystalline environment of Ce. The analysis of the main ESR resonance shows that the Ce^{3+} ions substitute for Sr^{2+} ones in the structure and permit the description of the electronic eigenfunctions and energy splitting of its $^2F_{5/2}$ ground state. We have tackled the distortion of the trigonal crystalline environment, induced by Na^+ codopants acting as charge compensators to Ce^{3+}, and we have assigned the ESR resonances to Na occupying sites at various distances from the Ce atoms. Our results indicate growth of high quality crystals. © *2003 American Institute of Physics.* [DOI: 10.1063/1.1542917]

I. INTRODUCTION

$LiSrAlF_6$ (LiSAF) crystals doped with Cr^{3+} and Ce^{3+} have recently attracted much interest as laser gain materials,[1,2] with potential use in various medical, industrial, environmental, and many other scientific applications. The Cr-doped LiSAF crystals present optical bands in the visible spectral region allowing efficient pumping by visible laser diodes. Among their advantages are their high tunability and their potential for generation of ultrashort laser pulses in the near infrared spectral range. In comparison with the isostructural Cr:$LiCaAlF_6$ (LiCAF), Cr:LiSAF offers the advantage of higher absorption coefficients and a broader tuning range,[1,2] however, the thermal quenching is stronger and leads to a shorter Cr fluorescence lifetime.[3] Ce:LiSAF and Ce:LiCAF are also very attractive because of their ultraviolet (UV) laser emission. Therefore, it is anticipated that an understanding of the structural and electronic characteristics of the doped LiSAF will allow the development of high quality and efficient flash- or diode-pumped UV and visible tunable lasers.

The crystal structure of both materials, LiCAF and LiSAF, has been examined by early x-ray diffraction (XRD) studies,[4,5] showing that both crystals have the same trigonal symmetry, with LiSAF exhibiting a larger $c-a$ anisotropy. Nevertheless, neither the atomic oscillations nor the effect of doping on the material's dynamical properties have been studied up to now.

On the other hand, the local crystalline environment of the dopant ions has been examined in detail because of its role in the material's optical and lasing properties. A very useful tool in such studies has been proved to be the electron spin resonance (ESR) spectroscopy. ESR investigations of Cr doped $LiSr_xCa_{1-x}F_6$,[6] LiSAF,[7] and LiSCaF mixed crystals[6] have described in detail the Cr site axial distortion and its dependence on disorder and temperature. In combination with optical measurements, the ESR data were used to determine the electronic energy diagram of the Cr^{3+} ions.

The Cr^{3+} dopants in LiSAF and LiCAF take the place of the Al^{3+} ions, which have similar ionic radii ($r_i=0.76$ Å for Cr^{3+} and 0.67 Å for Al^{3+}); the above substitution does not require any charge compensation. On the other hand, the Ce^{3+} ions, with $r_i=1.15$ Å, substitute for either the Ca^{2+} ($r_i=1.00$ Å) or the Sr^{2+} ($r_i=1.18$ Å) ones. Therefore, the Ce^{3+} ions are sixfold coordinated to neighbor F^- ions, forming a strongly trigonally distorted octahedral crystal field with the S_6 symmetry. The excess positive charge introduced by the Ce^{3+} atom is most probably charge compensated by Li^+ vacancies. If these vacancies are placed near the Ce atoms, their local crystalline symmetry is further distorted changing from trigonal to orthorhombic. In such a way, resonances with orthorhombic symmetry were identified in the ESR spectra of the LiCAF compound.[8] The orthorhombic distortion was also observed by splittings and broadenings of the optical absorption and luminescence spectra.[8,9] The role of Li vacancies is crucial since they can possibly act as color centers.[10] The presence of color centers causes a strong light absorption, which is anticipated to be detrimental to efficient laser performance. This mechanism is known as the solarization effect. In comparison to the Ce-doped LiCAF crystal, Ce-doped LiSAF generally suffers more from solarization losses, which results to a less favorable laser performance.[10]

The incorporation of Na^+ in the crystal is often used for charge compensation purposes, in order to diminish the alternative mechanism of the Li vacancies creation. The Na^+ ions are expected to replace Sr^{2+}, since they have a similar ionic radius. Sodium has also been used in order to prevent

[a]Author to whom correspondence should be addressed; electronic mail: akontos@central.ntua.gr

the creation of vacancies in Ce:$BaMgF_3$[11] and Ce:$BaMgF_4$,[12] and it was found to reside mainly in close distances to the Ce atoms.

This study is divided into two parts. First, we have carried out a comparative to Ce:LiCAF ESR study of the LiSAF compound, keeping, whenever possible, the notation used in Ref. 8. Second, we have identified the Raman modes of the LiSAF compound and we have examined the role of Cr and Ce doping on the material's properties. Finally some conclusions are presented in relation to the optical properties of the material.

II. EXPERIMENTAL TECHNIQUE

Undoped and Ce-doped LiSAF crystals have been grown using the Czochralski method. Cerium was codoped with sodium with concentrations of 0.5 mol % in the starting material. The final concentration is anticipated to approximately 0.007 mol % for Ce and 0.02 mol % for Na.[13] Cr:LiSAF single crystals doped with 1.5 and 3.5 mol % of Cr have been grown using the zone melting method.[14]

The optical axis of the crystals was determined by taking polarization measurements. Each sample was placed inbetween two crossed polarizers. An intense light source was focused on the sample by placing a long distance focal lens in front of the first polarizer and a fluorescent screen behind the second one. The sample was rotated around different axes, each one oriented along the direction of the light propagation. The *c* axis was identified on its orientation parallel to the rotation axis by its property of not affecting the polarization of the light that was crossing the sample independently of the rotation angle. Thus the incident polarized light was fully blocked by the last polarizer and it was not detected on the screen.

The ESR measurements were carried out at 11 K and $\approx$9.4 GHz (*X* band) in a Varian spectrometer. The sample was initially aligned with its *c* axis approximately parallel to the magnetic field ($\omega=0$); then, it was rotated about on an axis perpendicular to the $c-a$ plane, for $\omega=0°-90°-180°$, (i.e., where ω is the angle between the *c* axis and the direction of the magnetic field that is always lying on the $a-c$ plane). A detailed set of measurements was recorded in the range of 60°–120° where multiple peaks were detected in the ESR spectra. Subsequently, the temperature was raised up to 70 K under the control of a heater wound around the cavity and the ESR signal in the $c\|B$ direction was detected in steps of about 5°.

Raman measurements were carried out on a triple spectrometer (Jobin–Yvon T64000) in the backscattering configuration. A light beam at a wavelength of 514.5 nm was focused on the sample in a spot size of 1 μm and a charge coupled device (CCD) camera detected the Raman signal. An Ar lamp reference signal was also recorded in each measurement in order to calibrate the frequency scale. The instrumental resolution was equal to $\pm$ 0.3 cm^{-1}.

III. EXPERIMENTAL ESR AND RAMAN RESULTS

Characteristic ESR spectra of the Ce:Na:LiSAF crystal, measured at different angles ω, are shown in Fig. 1. For ω near 0° and 180°, three different peaks are clearly observed in the spectra. To the contrary, for the intermediate angles ω, the ESR spectra are rich of resonance lines; the maximum number of peaks and the broader resonance field range were observed for angles near 90°. All these peaks are interpreted as being due to Ce atoms in different crystalline environments due to the presence of Na charge compensators at different relative distances. The various peaks, *A*, *B*, *C*, and *D*, correspond to different Na positions according to the interpretation referred to in the following section. While the strong *A* resonance dominates all spectra with a single line, the *B* and *D* resonances are split in two lines having a ratio of about 1:2 and superimposed onto one line for angles adjacent to 0°. The 1, 2, or 3 multiplicity of the *B* and *D* lines is marked in Fig. 1 by a corresponding superscript index. The most intense satellite *B* and *C* lines can be identified in all the spectra and have a ratio of about 3:1. The abovementioned intensity ratios are more or less preserved for all the different angles and they are used as a criterion for the identification of the different resonances. The ω dependence of the various resonance lines has been grouped in plots (a) and (b) of Fig. 2 for the *A* and *B* resonances and plots (a) and (b) of Fig. 3 for the *C* and *D* ones, correspondingly.

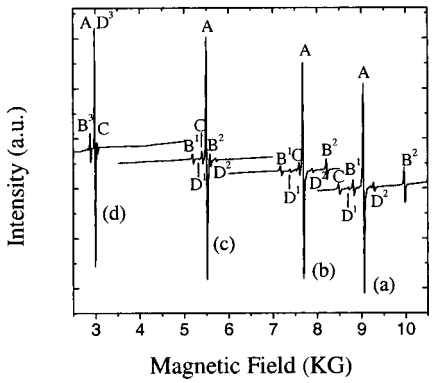

FIG. 1. Characteristic ESR spectra taken at 11 K, with the magnetic field in the $a-c$ plane at four different angles ω with reference to the *c* axis: (a) 92.5°, (b) 102.5°, (c) 117.5°, and (d) 184°. The spectra have been shifted vertically for clarity. Different resonance lines have been attributed to different local crystalline environments of the Ce atoms. The superscript index indicates degeneracy of resonances *B* and *D* into one, two, or three lines.

In Fig. 4 we have plotted the linewidth ΔH of the main resonance *A* line relative to the absolute temperature *T*. An exponential increase of ΔH upon increasing *T* is observed, which suggests the Orbach process as the dominant spin lattice relaxation mechanism.[15,16] Accordingly we get

$$\Delta H = a + b \exp\left(-\frac{\Delta E}{k_B T}\right), \tag{1}$$

where k_B is the Boltzman constant and ΔE is the energy difference between the ground and the first excited electronic state. A substitution of our data to Eq. (1) results in $\Delta E = 149 \pm 5$ cm^{-1}, with fitting parameters $a = 18.6 \pm 0.5$ G and $b = 376 \pm 50$ G.

Raman spectra were recorded with incident and scattered light parallel to the *c* and *a* axis, in all possible combinations (*a-a*, *c-c*, *a-c*). All samples, including that of the undoped reference, show the same Raman modes without any remark-

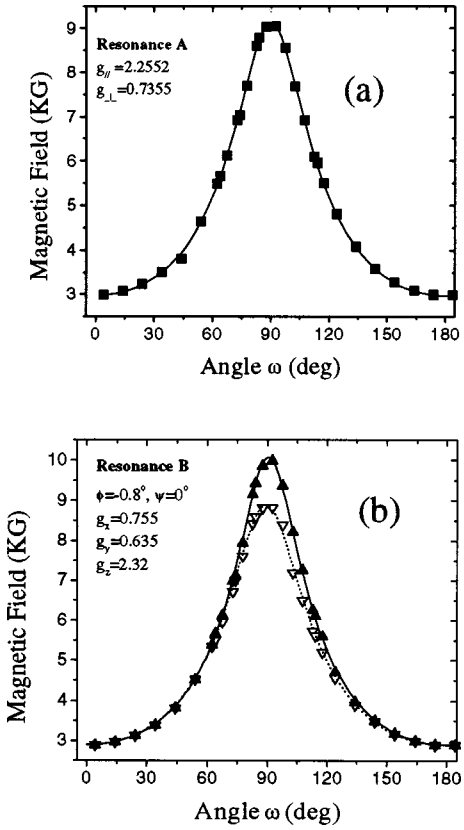

FIG. 2. (a) The dependence of the *A* ESR resonance peak position vs the angle ω between the direction of the *c* axis and that of the external magnetic field. The fitting curve considers an axial *g* tensor. (b) The same for the *B* resonance. In this case the fitting is done with a rhombic *g* tensor. The solid (open) symbols correspond to the doubly (singly) degenerate line, respectively.

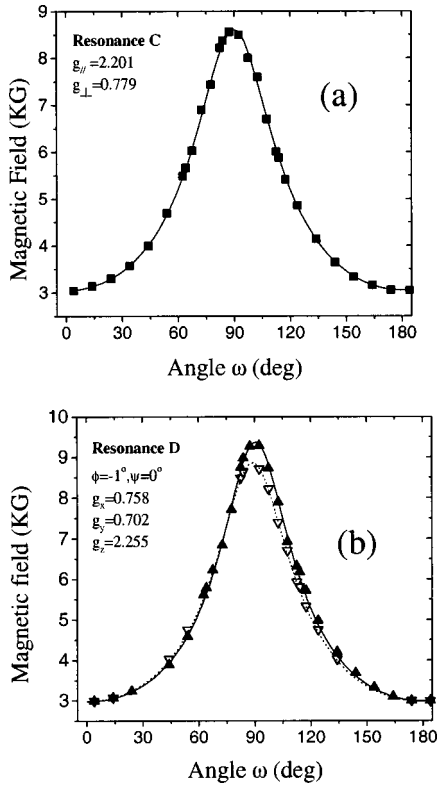

FIG. 3. The angle dependence of the ESR resonance lines, which were assigned to the axially symmetric *C* resonance (a) and the orthorhombic one *D*. (b) The solid (open) symbols stand for the doubly (singly) degenerate line, respectively. The solid lines are fittings taking an axial (a) and a rhombic (b) *g* tensor, correspondingly.

able differences. Characteristic spectra of the undoped sample are shown in Fig. 5. Eleven Raman modes were detected in the spectra at the frequencies 80, 141, 234, 251, 322.5, 377.5, 410, 437.5, 561.7, 578.5, and 843 cm^{-1}. Under crossed polarizations the modes at 251 and 377.5 cm^{-1} had almost vanished while the strongest mode at 561.7 cm^{-1} was reduced below 10% of its magnitude under the parallel $c-c$ polarization.

IV. DISCUSSION

A. The *g* tensor and the assignment of the various ESR resonances

The resonance position of the most intense *A* peak in the ESR spectra [Fig. 2(a)] presents an angular dependence with an axially symmetric effective $g(\omega)$ tensor defined as

$$g(\omega)=(g_{\parallel}^2\cos^2\omega+g_{\perp}^2\sin^2\omega)^{1/2}. \quad (2)$$

By fitting our experimental data to the above equation we get $g_{\parallel}=2.255\pm0.004$ and $g_{\perp}=0.735\pm0.005$. The excellent fitting of the *A* line to Eq. (1) shows that the *A*-type Ce site preserves a trigonal symmetry. This indicates that Ce, in this case, is quite isolated from nearby Na^+ ions. For illustrative purposes, a LiSAF unit cell, which hosts a Ce^{3+} ion at a Sr^{2+} site, has been drawn in Fig. 6(a), where the *A* position of a Na^+ charge compensating ion in a far distance is marked.

The behavior of the resonance site *B* in Fig. 1 suggests a Ce lattice site with orthorhombic symmetry. Considering the orthorhombic environment as a superposition of the initial distorted along the-*c* octahedral system (*abc*) with another axially symmetric distortion (along an arbitrary c'), the final biaxial *g* tensor ellipsoid has its two principal axes on the $c-c'$ plane. Therefore, the orthorhombic system *xyz* can be

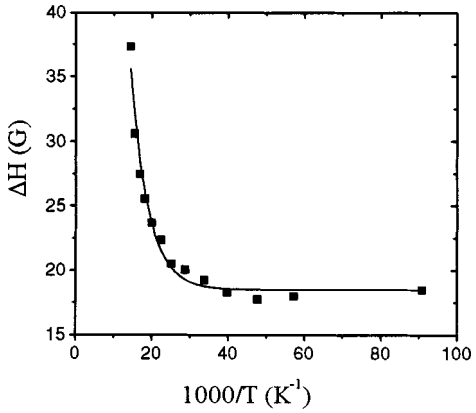

FIG. 4. The inverse temperature dependence of the main ESR resonance linewidth undertaken with *B* parallel to the *c* axis.

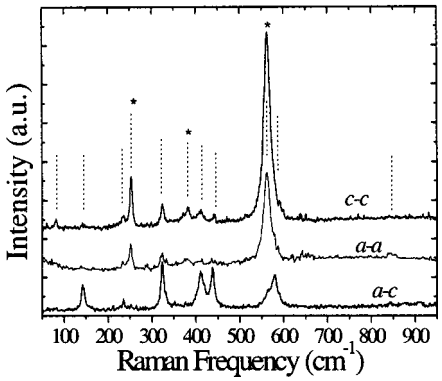

FIG. 5. The Raman spectra of the undoped LiSAF crystal recorded with parallel *c-c* and *a-a* and crossed *a-c* polarizations of the incident and scattered beams. The observed bands are marked with vertical lines. The bands that are substantially reduced in the *a-c* configuration are marked by stars.

defined with respect to *abc* with two angles, as shown in Fig. 6(b): (a) φ angle between *c* and *z* and (b) ψ angle between *a* and the projection of *z* to the $a-b$ plane.

The angular dependence of a resonance line in the orthorhombic environment is described by a spin Hamiltonian[15]

$$H_s=\mu_B g_x B_x S_x+\mu_B g_y B_y S_y+\mu_B g_z B_z S_z. \tag{3}$$

The effective *g* value is given now by

$$g^2=g_x^2 l^2+g_y^2 m^2+g_z^2 n^2, \tag{4}$$

where *l*, *m*, and *n* are the direction cosines of the magnetic field relative to the *xyz* system axes, i.e.,

$$1=\sin\omega\cos\varphi\cos\psi-\cos\omega\sin\varphi, \tag{5a}$$

$$m=-\sin\omega\sin\psi, \tag{5b}$$

$$n=\sin\omega\sin\varphi\cos\psi+\cos\omega\cos\varphi. \tag{5c}$$

Each lattice distortion by a dopant or a vacancy in a neighboring to Ce lattice site can produce a distinct crystal field environment. For each distortion the equivalent sites are taken into account by applying the site symmetry operations of the Ce atom. In this way, such distortions that produce a single line for $c\|B$ can reveal up to three different lines for $c\perp B$, as it was observed in LiCAF,[8] due to the presence of Li vacancies near the Ce atoms.

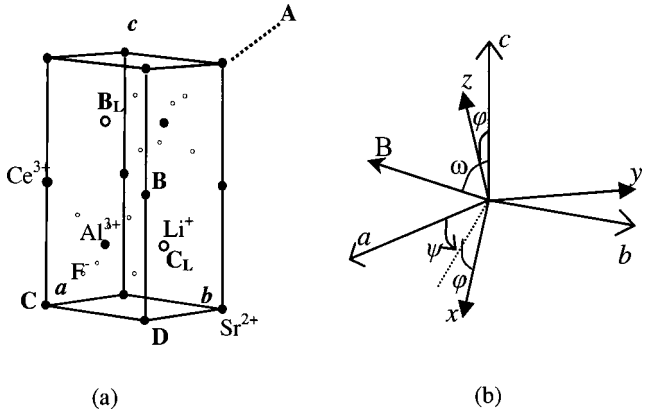

FIG. 6. (a) A schematic diagram of the $LiSrAlF_6$ crystal structure. *A* label indicates a Na atom lying far from the Ce dopant position. *B*, *C*, and *D* labels show the Na^+ sites up to third neighbors to a Ce dopant. B_L and C_L stand for the first and second neighbors to the Ce lattice sites of Li^+ vacancies. (b) A drawing of the principal crystalline axes system, where the magnetic field is in the $c-a$ plane and points at an angle ω to the *c* axis. The transformation of the axes is shown for an orthorhombic environment at arbitrary angles φ and ψ relative to the principal axes system.

As shown in Fig. 2(b), the *B* peak indicates, in a good approximation, a symmetric variation around the $\omega=90°$ and a systematic splitting into two lines with an approximate 1:2 ratio (see Fig. 1). This suggests that we have a special case where two of the three lines, which are expected in general, are superimposed. This case appears only when the system axes, which describe the orthorhombic distorted environment, are near the high symmetry directions of $\varphi=0°$ and $\psi=0°$ (also $\psi=120°$ and 240°, for the equivalent crystallographic sites) or $\psi=30°$ (also $\psi=150°$ and 270°) relative to the crystallographic system. This is somehow expected since the trigonal distortion of the crystal in the *c* direction is very strong and it is hardly affected by the Na^+ substituting ions. Therefore the *z* axis almost coincides with the *c* axis and g_z remains the larger component of the *g* tensor. On the other hand, the Na^+ ions are responsible for the orthorhombic distortion of the axial environment in their direction relative to Ce, i.e., the Sr–Sr bond direction, which for adjacent Sr sites up to the third neighboring distance, sets at $\psi=0°$. Under these assumptions we have solved Eqs. (4) and (5) for the *B* resonance data in Fig. 2(b) getting $\varphi=-0.8°$, $\psi=0°$, $g_x=0.755\pm0.008$, $g_y=0.635\pm0.008$, and $g_z=2.320\pm0.008$. The above resonance shows the maximum deviation from the inherent trigonal crystal field and the strongest orthorhombic distortion. Thus, it is attributed to the closest $Ce^{3+}-Na^+$ position, namely the first neighboring Sr positions in the $a-b$ plane, marked as *B* sites in Fig. 6(a). Moreover, this resonance is quite intense, implying a preference of the Na^+ to be placed near the Ce site.

Correspondingly, the *C* site is attributed to the second neighboring Na ion position, which is that of the Sr neighboring atoms in the *z* direction [see Fig. 6(a)]. These atoms are only in slightly larger distances than the *B* ones. However, the *C*:*B* coordination number ratio is 2:6, i.e., 1:3; this is the ratio of the *C*:*B* peak intensities in the ESR spectra. Due to the distortion of the crystal field environment in the trigonal axis, the *C* resonance appears with a single line, in the same way as the resonance *A* behavior, having an effective axial *g* tensor equal to $g_\|=2.201\pm0.005$ and $g_\perp=0.779\pm0.005$.

The *D* resonance has the characteristic split behavior of the *B* one. The treatment according to Eqs. (4) and (5) yields $\varphi=-1°$, $\psi=0$, and $g_x=0.758\pm0.015$, $g_y=0.702\pm0.015$, and $g_z=2.255\pm0.005$. Accordingly the *D* resonance lines are attributed to Na sites at the third neighboring distances from Ce, i.e., the diagonal Sr sites in the $a-b$ plane as shown in Fig. 6(a).

Finally, very weak resonance lines were observed in the spectra obtained near $\omega=90°$, which may be attributed to Na ions in intermediate distances from *A* and *D* sites. Remarkably, Li vacancies near the Ce atoms were not detected by ESR, since in this case the crystal field distortion would be very strong with resonance lines in a broad resonance field range.[8]

TABLE I. The numerical principal values of the effective g tensor and the coefficients of the ground state electronic eigenfunctions deduced from the positions of the Ce^{3+} ESR resonances in Ce:LiSAF. The values in parenthesis correspond to Ce:LiCAF.[a] For the positions *A, B, C,* and *D* of the Na^+ ions and B_L, C_L of the Li vacancies relative to a Ce dopant, refer to Fig. 6(a).

	A	(A)	B	(B_L)	C	(C_L)	D
g_x	0.735	(0.965)	0.755	(0.95)	0.779	(0.84)	0.758
g_y	0.735	(0.965)	0.635	(1.27)	0.779	(1.18)	0.702
g_z	2.255	(1.725)	2.320	(1.54)	2.201	(1.77)	2.255
g_{rat}	3.068	(1.788)	3.338	(1.387)	2.825	(1.753)	3.089
$\vartheta_{\text{av}}(^\circ)$	54.7	(48.4)	56.0	(45.5)	54.0	(48.2)	55.1
α	0	(0)	0.022	(0.047)	0	(0.053)	0.010

[a]See Ref. 8.

The relative intensities of the ESR lines can be used in order to estimate the probability for Na to occupy one of the Sr sites. The intensity ratio $(B+C)/(A+B+C+D)$ (Fig. 1) leads to an occupation probability for a Na atom, in one of the six Sr neighboring sites around a Ce dopant (sites *B* and *C*), of about 21%. Taking into account the actual Na concentration of approximately 0.02% in the sample, the above probability is over 1000 times that expected upon a random distribution of Na in the crystal. In a similar manner, the occupation probability for the *D* site, deduced from the partial intensity $D/(A+B+C+D)$ in Fig. 1, is about 5%.

B. The ground electron state and the crystal field distortion by Na^+ charge compensators

The ground state of the Ce^{3+} free ion is ^2F. Under the spin–orbit interaction, the ^2F state is split into the $^2F_{5/2}$ ground state and the $^2F_{7/2}$ one, which lies about 2200 cm^{-1} higher. This difference is much greater than the energy splitting produced by the crystal field. So, in a first approximation, we take the total angular momentum $J=5/2$ as a good quantum number.[15,16] The corresponding electronic eigenfunctions are represented as Kramers doublets $|J,J_z\rangle$ i.e., $|\frac{5}{2}, \pm\frac{1}{2}\rangle$, $|\frac{5}{2}, \pm\frac{3}{2}\rangle$, and $|\frac{5}{2}, \pm\frac{5}{2}\rangle$.

The crystal field Hamiltonian in the trigonally distorted octahedral symmetry is expressed as[15,16]

$$H_{\text{cry}}=B_2^0O_2^0+B_4^0O_4^0+B_4^3O_4^3, \tag{6}$$

where O_n^m are Steven's spin operators and B_n^m are crystal field parameters.

The energy diagram of the Ce atom in the H_{cry} of Eq. (6), is represented by three defined Kramers doublets

$$|\pm\overline{\tfrac{1}{2}}\rangle=\cos\vartheta|\tfrac{5}{2},\pm\tfrac{1}{2}\rangle\pm\sin\vartheta|\tfrac{5}{2},\mp\tfrac{5}{2}\rangle, \tag{7a}$$

$$|\pm\overline{\tfrac{3}{2}}\rangle=|\tfrac{5}{2},\pm\tfrac{3}{2}\rangle, \tag{7b}$$

$$|\pm\overline{\tfrac{5}{2}}\rangle=\sin\vartheta|\tfrac{5}{2},\pm\tfrac{1}{2}\rangle\mp\cos\vartheta|\tfrac{5}{2},\mp\tfrac{5}{2}\rangle, \tag{7c}$$

at different energies.

The effective g factors of the ground state are obtained by calculating matrix elements of the form $\langle\pm\overline{\frac{1}{2}}|H_z|\pm\overline{\frac{1}{2}}\rangle$ i.e., where H_z is the Zeeman interaction.

In the approximation of treating the $^2F_{5/2}$ independently

$$H_Z=g_L\mu_B\mathbf{J}\cdot\mathbf{B}, \tag{8}$$

where μ_B is the Bohr magneton and $g_L=6/7$ is the Landé factor for the $^2F_{5/2}$ state.

Accordingly, the effective g factor for the $|\pm\overline{\frac{1}{2}}\rangle$ is calculated as

$$g_\perp=3g_L\cos^2\vartheta \tag{9a}$$

and

$$|g_\parallel|=g_L(5\sin^2\vartheta-\cos^2\vartheta). \tag{9b}$$

The orthorhombic distortion introduced by the Na^+ ions in nearby sites to Ce is taken into account by the introduction of an extra term $B_2^2O_2^2$ in the crystal field Hamiltonian.[15,16] The new term is considered as a perturbation of the terms in Eq. (6). The expected ground state electron eigenfunction results from the $|\pm\overline{\frac{1}{2}}\rangle$ in Eq. (7) slightly modified by the admixture of the other states in the same equation as

$$|\pm\widetilde{\tfrac{1}{2}}\rangle=N(|\pm\overline{\tfrac{1}{2}}\rangle+\alpha|\mp\overline{\tfrac{3}{2}}\rangle\pm\beta|\mp\overline{\tfrac{5}{2}}\rangle), \tag{10}$$

where N is a normalization factor.

Assuming that the admixture coefficients α and β are very small and calculating the matrix elements $\langle\pm\widetilde{\frac{1}{2}}|H_z|\pm\widetilde{\frac{1}{2}}\rangle$, we end up with the following effective g values for the ground state $|\pm\widetilde{\frac{1}{2}}\rangle$:[8,15]

$$g_x=g_L(3\cos^2\vartheta+4\sqrt{2}\alpha\cos\vartheta), \tag{11a}$$

$$g_y=g_L(3\cos^2\vartheta-4\sqrt{2}\alpha\cos\vartheta), \tag{11b}$$

$$|g_z|=g_L(5\sin^2\vartheta-\cos^2\vartheta). \tag{11c}$$

The difference g_x-g_y can be merely found equal to $8\sqrt{2}g_L\alpha\cos\vartheta$. Evidently for a trigonal field, $\alpha=0$ and the solutions of g coincide with those of Eq. (9).

In Table I we present the g values of the different resonances, which have been obtained in this study. The corresponding values for LiCAF, obtained in Ref. 8, are also presented for comparison. The anisotropy of the main *A* resonance in LiSAF is much higher than its counterpart in LiCAF. This shows a higher elongation of the Ce octahedral environment in LiSAF in comparison to LiCAF, in agreement with the XRD data.[4,5]

For the estimation of the eigenfunction coefficients in Eq. (7a) we have calculated an average ϑ value equal to $\vartheta_{\text{av}}=\tan^{-1}\sqrt{(3g_{\text{rat}}+1)/5}$ through Eq. (9), where $g_{\text{rat}}=|g_\parallel|/g_\perp$. From the experimental g ratios a $\vartheta_{\text{av}}=54.7^\circ$ was

estimated for the *A* line to be compared with $\vartheta_{av}=48.4°$ for LiCAF and $\vartheta=41.8°$ for the regular isotropic environment, where g is isotropic and equal to $|g|=\frac{5}{3}g_L$. These results, together with Eq. (7a), show that the $|\frac{5}{2},\mp\frac{5}{2}\rangle$ state becomes progressively more important in the ground state combination as we move from the isotropic case to LiCAF and then to LiSAF.

In the same manner we have calculated ϑ_{av} for the *B*, *C*, and *D* resonances; for *B* and *D*, instead of $g_\perp$ the mean value of g_x and g_y has been used. These ϑ_{av} values are also shown in Table I. Since the Na^+-Ce^{3+} electrostatic repulsive interaction is weaker than the $Sr^{2+}-Ce^{3+}$ one, the *B* resonance (Ce–Na bond in the *a* direction) is expected to represent an elongation of the octahedral Ce environment, while the *C* resonance (Ce–Na bond in the *c* direction) represents a compression. This is in accordance with the ϑ_{av} values for *B* and *C* resonances recorded in Table I where, moreover, as the Na ions draw away from the Ce dopants occupying sites $B-C-D$, the ϑ_{av} values approach those of the *A* resonance. As for the calculated α coefficient in Table I, its value for the *D* resonance is about half of that of the *B* one. All these results verify the progressive attenuation of the crystal field distortion by Na far from the Ce atoms and the self consistency of the ESR resonance lines assignment. Experimental ESR results in Ce:LiCAF without Na charge compensators are also presented in Table I for comparison. Charge compensation by Li^+ vacancies in the first (B_L) and second (C_L) neighbors to Ce positions was also detected; the Li sites are marked in Fig. 6(a) too. From the values of Table I we deduce that the distortion of the trigonal Ce environment by Li vacancies is much more intense compared to that induced by the Na^+ ions. In this last case the obtained ϑ_{av} values approach those of the *A* resonance and the mixing coefficient α becomes very small. This suggests that the Na atoms do not alter the energy diagram, significantly and thus the Na codoped Ce:LiSAF crystals are expected to show less inhomogeneous broadening and multiple lines in the absorption and luminescence spectra relative to the Ce:LiSAF ones. Such effects were observed, for example, in the luminescence spectra of Ce:LiCAF[8] and Ce:$BaLiF_3$[11] while they were reduced in those of the Na codoped Ce:$BaLiF_3$.[11]

C. The Raman modes and the effect of doping

LiSAF has trigonal symmetry and belongs to the D_{3d}^2 symmetry space group which has, according to Wyckoff's notation, the following symmetry elements:[17]

$$\infty[iC_1(12)]+\infty[hC_2(6)]+gC_i(6)+\infty[(f+e)C_3(4)]+(d+c+a)D_3(2)+bS_6(2). \quad (12)$$

In LiSAF, Li and Al occupy the D_3 site, Sr the S_6 site, and *F* the C_1 site. The lattice modes, which correspond to each of these site groups, are

$$D_3: A_{2g}+A_{2u}+E_g+E_u, \quad (13a)$$

$$S_6: A_{1u}+A_{2u}+2E_u, \quad (13b)$$

$$C_1: 3A_{1g}+3A_{1u}+3A_{2g}+3A_{2u}+6E_g+6E_u. \quad (13c)$$

On the whole, we expect the material to have the following lattice modes:

$$3A_{1g}+4A_{1u}+5A_{2g}+6A_{2u}+8E_g+10E_u. \quad (14)$$

From these modes the A_{1u} are silent, the A_{2g} only infrared active, and the A_{2u} and E_u are acoustical modes. Finally the remaining $3A_{1g}+8E_g$ modes, 11 in total, are Raman active and were all identified in our spectra.

According to the selection rules of the backscattering geometry, under parallel polarizations of the incident and scattered beam in the *c* axis ($c-c$), only the A_{1g} modes are expected in the Raman spectra, while in the crossed polarization configuration ($a-c$), only the E_g ones. In the $a-a$ configuration all the modes are expected. Indeed, we have observed three modes at 251, 377.5, and 561.7 cm^{-1}, which are strong only in the $c-c$ configuration. These modes are assigned to the A_{1g} symmetry and result from the motion of the *F* atoms in the *z* direction, while the other atoms remain at rest. On the contrary, the selection rules for the remaining eight E_g modes do not apply strictly. The reason for this is not yet well understood; it is probably related to the large solid angle of scattered light collected by the microscopic lens in combination with the multiple internal reflections of the excitation beam within the transparent plate-like sample. A further clarification will hopefully be given in the future by comparative Raman studies in LiCAF.

Finally it should be mentioned that the doping does not affect appreciably the Raman spectra, which verifies that the material is not subject to strong stresses that could alter the resonance frequencies or to disorder effects which would cause severe line broadening.[18] These results suggest low tensions, deformations, and variations of the refractive index along the optical axis and a minimum level of inhomogeneities during the crystallization process that have been proposed to be responsible for the formation of color centers.[19] Together with the absence of vacancies detectable in the ESR spectra, our crystals show a high structural quality and are promising for high laser efficiency without severe solarization losses.

V. CONCLUSIONS

ESR measurements of Ce doped $LiSrAlF_6$ single crystals have shown that Ce resides mainly in an axially symmetric Sr position. The effective *g* factor of this Ce resonance has been determined and conclusions have been drawn for the electronic eigenfunctions, which describe the ground state energy level. Ce resonances due to Ce sites with orthorhombic symmetry have been detected in the ESR spectra with multiple lines. These resonances have been attributed to charge compensating Na^+ ions, which perturb the crystal field environment at Ce sites in the direction of the Sr–Sr bonds. ESR resonances, which result from up to the third neighboring Na to Ce sites, have been identified and the principal values of the corresponding *g* tensors have been estimated. Nonetheless, the crystal field distortion in the *c* axis remains the dominant one and determines, by a maximum deviation of 1°, the one principal axis direction of the *g* tensor. The effective *g* factor of these resonances as well as

the Na^+ occupation sites and probabilities have been estimated and are further correlated to the material lasing properties, always in comparison to the isostructural $LiCaAlF_6$. The energy splitting between the ground and the first excited electronic states has been estimated by the temperature dependence of the ESR linewidths.

Undoped as well as Cr and Ce doped LiSAF crystals were further examined for their lattice dynamical properties. Polarized Raman measurements have been combined with group theoretical arguments in order to identify the observed lattice vibrational modes. Strain or disorder effects were not detected in the Raman spectra.

ACKNOWLEDGMENTS

The authors wish to thank Dr. N. Ioannidis and Dr. V. Petrouleas from the NCSR Democritos for allotting their ESR facility and for their help with the measurements and Dr. V. Likodimos for helpful discussions. They gratefully acknowledge partial financial support by NTUA.

[1] M. Stalder, B. H. T. Chai, and M. Bass, Appl. Phys. Lett. **58**, 216 (1991).
[2] C. D. Marshall, J. A. Speth, S. A. Payne, W. F. Krupke, G. J. Quarles, V. Castillo, and B. H. T. Chai, J. Opt. Soc. Am. B **11**, 2054 (1994).
[3] M. Stalder, M. Bass, and B. H. T. Chai, J. Opt. Soc. Am. B **9**, 2271 (1992).
[4] V. W. Viebahn, Z. Anorg. Allg. Chem. **386**, 335 (1971).
[5] K. I. Schaffers and D. A. Keszler, Acta Crystallogr., Sect. C: Cryst. Struct. Commun. **C47**, 18 (1991).
[6] M. Yamaga, B. Henderson, K. Holliday, T. Yosida, M. Fukui, and K. Kindo, J. Phys.: Condens. Matter **11**, 10499 (1999).
[7] A. N. Medina, A. C. Bento, M. L. Baesso, F. G. Gandra, T. Catunda, and A. Cassanho, J. Phys.: Condens. Matter **13**, 8435 (2001).
[8] M. Yamaga, D. Lee, B. Henderson, T. P. J. Han, H. G. Gallagher, and T. Yosida, J. Phys.: Condens. Matter **10**, 3223 (1998).
[9] N. Kodama, M. Yamaga, and B. Henderson, J. Appl. Phys. **84**, 5820 (1998).
[10] A. J. Bayramian, C. D. Marshall, J. H. Wu, J. A. Speth, S. A. Payne, G. J. Quarles, and V. K. Castillo, J. Lumin. **69**, 85 (1996).
[11] M. Yamaga, T. Imai, K. Shimamura, and T. Fukuda, J. Cryst. Growth **229**, 487 (2001).
[12] N. Kodama, T. Hoshino, M. Yamaga, N. Ishizawa, K. Shimamura, and T. Fukuda, J. Cryst. Growth **229**, 492 (2001).
[13] V. L. Mazzocchi (private communication).
[14] M. C. H. M. Ruiz, E. A. Barbosa, E. P. Maldonado, S. P. Morato, N. U. Wetter, N. D. Vieira, Jr., and S. L. Baldochi, J. Cryst. Growth **241**, 177 (2002).
[15] J. W. Orton, *Electron Paramagnetic Resonance* (Pitman, London, 1968).
[16] A. Abragam and B. Bleaney in *Electron Paramagnetic Resonance of Transition Ions* (Dover, New York, 1986), Chap. 3.
[17] D. L. Rousseau, R. P. Bauman, and S. P. S. Porto, J. Raman Spectrosc. **10**, 253 (1981).
[18] F. H. Pollak, in *Analytical Raman Spectroscopy*, edited by J. Granspelli and B. Bulkin (Wiley, New York, 1991), Chap. 6
[19] H. Sato *et al.*, Jpn. J. Appl. Phys., Part 1 **41**, 2028 (2002).